remote sensing

MDPI

Article

Scale-Dependent Agreement of Hydrological Loading Displacements from GNSS, GRACE, and a Land Surface Model in the Heihe River Basin

Jingzun Mao [1], Yue Gao [2], Jianmin Bian [1,3], Jongmin Park [4], Yaohui Nan [2,4,5], Rongchang Zhao [2,4,5] and Gaohong Yin [1,3,*]

[1] Key Laboratory of Groundwater Resources and Environment, Ministry of Education, Jilin University, Changchun 130021, China; jzmao25@mails.jlu.edu.cn (J.M.); bianjm@jlu.edu.cn (J.B.)
[2] Water Cycle Field Station of the Heihe River Basin, CGS, Zhangye 734023, China; gaoyue0917@163.com (Y.G.); cugnyh@163.com (Y.N.); ya59718@foxmail.com (R.Z.)
[3] Jilin Provincial Key Laboratory of Water Resources and Environment, Jilin University, Changchun 130021, China
[4] Department of Environmental Engineering, Korea National University of Transportation, Chungju 380-702, Republic of Korea; jmpark1@ut.ac.kr
[5] Gansu Inland Arid Area Water Cycle and Water Balance Field Scientific Observation and Research Station, Zhangye 734023, China
* Correspondence: gyin@jlu.edu.cn

Abstract

Ground-based Global Navigation Satellite System (GNSS) vertical displacements provide an independent measure of hydrological loading, but their ability to resolve terrestrial water storage (TWS) variations in arid inland basins remains uncertain. This study compared vertical displacements from 15 GNSS stations within and around the Heihe River Basin with loading displacements derived from satellite-based GRACE and model-based Noah TWS anomalies. After removing non-hydrological signals from GNSS series, correlations among the network-mean vertical displacement for GNSS-GRACE, GNSS-Noah, and GRACE-Noah were 0.48, 0.49, and 0.74, respectively. Mean station-level correlations for the same comparisons were lower (0.38, 0.35, and 0.60, respectively), with weaker agreement within the basin interior. Time-series decomposition showed that GNSS captured inter-annual TWS variability more consistently than the seasonal cycle of TWS. GNSS generally peaks earlier than GRACE in the south but later in the north. Noah inter-annual variations diverged from both GNSS and GRACE, suggesting limitations in the model's representation of arid-region hydrological processes. Overall, GNSS provides an independent constraint on long-term TWS variability and a diagnostic of land surface model performance. These findings support multisource monitoring of arid-basin water storage while highlighting the need for improved scale matching and in situ validation.

Keywords: terrestrial water storage; GNSS; GRACE; land surface model; Heihe River Basin

Academic Editor: Chung-yen Kuo

Received: 21 September 2026
Revised: 22 October 2026
Accepted: 23 October 2026
Published: 26 October 2026

Copyright: © 2026 by the authors. Licensee MDPI, Basel, Switzerland. This article is an open access article distributed under the terms and conditions of the Creative Commons Attribution (CC BY) license.

1. Introduction

Terrestrial water storage (TWS) comprises water stored in snow, soil moisture, surface water bodies, groundwater, and vegetation canopies. As an integrated variable of the terrestrial water cycle, TWS variations reflect the combined effects of climate variability

and human activities [1,2]. Reliable characterization of TWS is particularly important in drylands, where limited water availability constrains ecosystem functioning and socioeconomic development [3,4]. Several major hotspots of TWS decline are located in arid regions, such as the inland river basins of northwestern China [5–7]. The Heihe River Basin is a representative mountain-oasis-desert system in this region. Runoff generated in the Qilian Mountains sustains irrigated agriculture in the middle reaches and water-dependent ecosystems in the lower reaches, while irrigation, groundwater abstraction, and ecological water allocation redistribute water across the basins [8–10]. Continuous monitoring of TWS is therefore essential for assessing changes in regional water availability and understanding their climatic and anthropogenic drivers.

The Gravity Recovery and Climate Experiment (GRACE) and its successor, GRACE Follow-On (GRACE-FO; hereafter collectively referred to as GRACE), detect temporal variations in Earth's gravity field and have enabled large-scale estimates of terrestrial water storage anomalies (TWSA) [1,11]. However, the effective spatial resolution of GRACE is much coarser than its nominal grid spacing, resulting in spatially smoothed TWSA estimates that are susceptible to spatial leakage and boundary effects. These limitations are particularly important in relatively small or hydrologically heterogeneous basins, where contrasting local signals may be spatially averaged within the GRACE footprint. Land surface models provide continuous estimates of individual water storage components at finer spatial and temporal resolutions, but their simulations remain sensitive to meteorological forcing, model parameterizations, and process representations [12,13]. In particular, many land surface models often omit or inadequately represent deep groundwater storage or human activities such as irrigation, groundwater abstraction, and reservoir regulation. GRACE and land surface models therefore provide complementary information, but neither can fully resolve fine-scale TWS variations in intensively managed inland river basins.

The Global Navigation Satellite System (GNSS) observations provide an independent measure of crustal deformation associated with changes in terrestrial water mass. Under elastic loading, water accumulation generally produces downward surface displacement, whereas water loss results in uplift [14,15]. After appropriate corrections for non-hydrological loading effects, such as tectonic motion, atmospheric and oceanic loadings, GNSS vertical displacements have shown considerable potential for monitoring hydrological loading [16,17]. However, groundwater withdrawal can reduce pore pressure and induce the compaction of the aquifer system, resulting in land subsidence at GNSS stations overlying the affected aquifer, even though the associated reduction in water mass may produce elastic uplift at nearby stations [18,19]. Conversely, groundwater recharge may cause local uplift through aquifer expansion while producing elastic subsidence in the surrounding region due to the increased water load. Therefore, using GNSS vertical displacement to infer water mass variations across different regions requires careful assessment of the dominant deformation mechanisms.

Unlike GRACE, which represents spatially smoothed mass variations, each ground-based GNSS station records the integrated elastic response to surrounding water loads, with relatively high sensitivity to nearby mass changes and much finer temporal sampling. Previous studies have used GNSS to investigate hydrological loading in regions such as the western United States, the Himalayas, the Amazon Basin, and the southwestern China [20–23]. However, its ability to constrain TWSA depends strongly on loading magnitude and distribution, station geometry and observational noise. Whether GNSS can reliably capture the relatively weak and spatially heterogeneous hydrological signals of arid mountain-oasis-desert basins remains uncertain.

The Heihe River Basin provides a suitable setting for addressing this question because its upper, middle, and lower reaches are characterized by different hydrological

processes. Snow and soil water changes influence the mountainous headwaters, irrigation and groundwater abstraction affect the middle-reach oases, and ecological water allocation dominates the lower reaches. These spatially heterogeneous signals may be smoothed in GRACE retrievals and inadequately represented by land surface models. Although GNSS vertical displacement has been widely used to investigate hydrological loading, its applicability in arid inland basins with sparse GNSS coverage, weak regional water mass variations, and intensive water management remains insufficiently understood. Therefore, this study systematically evaluates the scale- and location-dependent capability of GNSS for monitoring hydrological loading variations under these conditions. Vertical displacements observed at GNSS stations within and surrounding the basin were compared with hydrologically induced vertical displacements derived from GRACE and Noah TWSA. Agreements among the three datasets at different spatial and temporal scales were quantified to identify common signals and systematic differences. This comparison further clarifies the capabilities and limitations of GNSS, GRACE, and Noah in representing hydrological loading in a data-sparse arid inland river basin.

2. Materials and Methods

2.1. Study Area

The Heihe River Basin is a representative arid inland river basin in northwestern China (Figure 1). Originating in the Qilian Mountains, the Heihe River flows northward through the Hexi Corridor and ultimately reaches the Alxa Plateau. Elevation decreases markedly from the mountainous headwaters in the south to the downstream desert plains in the north, resulting in pronounced hydroclimatic gradients across the basin [10,24].

Geologically, the basin spans the actively deforming Qilian Mountains at the northeastern margin of the Tibetan Plateau, the Hexi Corridor foreland basin, and the sedimentary Ejina Basin. The North Qilian Mountain Fault constitutes a major tectonic boundary between the mountains and the foreland basin. In the middle reaches, particularly in the Zhangye Basin, Quaternary alluvial and proluvial deposits form piedmont fans and river-valley plains. Farther downstream, the Ejina Basin is characterized by fluvial–alluvial, aeolian, and lacustrine deposits [25–27].

Precipitation and evaporative demand vary strongly across space. Previous studies have reported annual precipitation of approximately 200–500 mm in the upper reaches, less than 200 mm in the middle reaches, and generally below 50 mm in the lower reaches. In comparison, evaporation increases from about 700 mm in the upper basin to nearly 3000 mm downstream [28,29]. Vegetation and land cover vary correspondingly along this mountain-to-desert gradient [30]. Alpine meadows and mountain grasslands, together with patches of Qinghai spruce forests, dominate the upper reaches. Irrigated croplands and artificial oases are concentrated in the middle reaches and are interspersed with sparsely vegetated piedmont desert. Desert and bare land cover most of the lower reaches, while riparian Populus euphratica forests and Tamarix shrublands are largely confined to river corridors and groundwater-supported areas. This pronounced hydroclimatic and land surface heterogeneity has made the Heihe River Basin an important experimental region for integrated hydrological, ecological, and remote-sensing observations in the cold and arid regions of China [10].

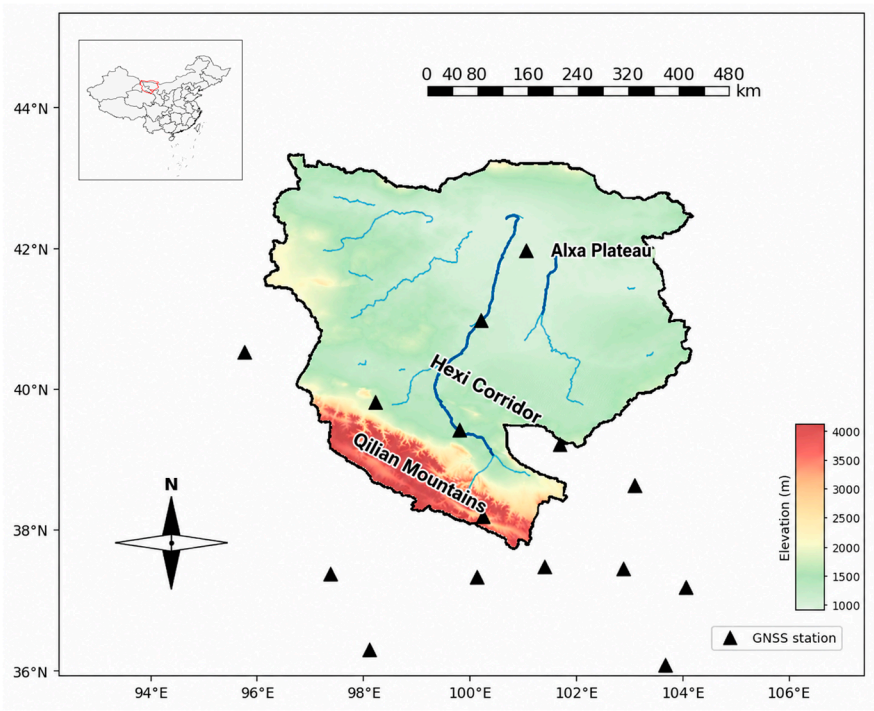


Figure 1. Location and topographic characteristics of the Heihe River Basin, with the distribution of GNSS stations marked in triangles.

The mountainous upper reaches constitute the principal runoff-generating region, with water supplied primarily by mountain precipitation, seasonal snowmelt, and glacier meltwater. In the middle reaches, river flow is substantially modified by irrigation withdrawals, evapotranspiration, and surface water-groundwater exchanges, while the remaining runoff sustains the terminal ecosystems of the lower reaches. Hydrological conditions in the middle and lower reaches are therefore dependent on both local climate and upstream runoff regulation [10,24]. These coupled natural and managed processes provide the hydrological context for differences among the loading displacements derived from GNSS, GRACE, and Noah.

2.2. Datasets

2.2.1. GNSS

Daily GNSS vertical displacements were obtained from the Crustal Movement Observation Network of China (CMONOC), with station information archived by the National Earthquake Science Data Center (http://data.earthquake.cn (accessed on 24 December 2025)). Fifteen stations within and around the Heihe River Basin were selected, including five stations inside the basin and ten in surrounding regions (Figure 1). The common analysis period extended from February 2012 to November 2023.

The detrended GNSS data were used in the study, and it is assumed to be related to glacial isostatic adjustment (GIA) and tectonic effects [31,32]. A series of steps were conducted to reduce non-hydrological signals following previous studies [16,17,33]. Offsets associated with earthquakes, antenna replacements, and other equipment-related events were identified from station metadata and corrected for each station. Outliers were then identified and removed based on three times the standard deviation relative to the mean of each time series. Afterward, vertical displacements caused by atmospheric and nontidal oceanic mass variations were removed using the Atmospheric and Ocean De-Aliasing (AOD) model [34]. The effects of thermal expansion of the station monuments and surrounding bedrock on the vertical time series were subsequently estimated and corrected following the method proposed by Yan et al. [35]. The GNSS time series used in

this study were linearly detrended prior to the removal of offsets and modeled non-hydrological effects. This order may introduce residual artificial trends if the subsequently removed corrections contain long-term components. A sensitivity experiment, in which the linear trend was removed after all corrections, showed only minor differences in the monthly GNSS displacements. Since both detrending strategies may remove a potential secular hydrological signal, this study focused on interannual and seasonal deformation and did not interpret the linear long-term trend. Future work should explicitly model and correct for GIA and tectonic motions, rather than absorbing these signals into an empirical linear trend.

The corrected daily GNSS vertical displacement series were averaged on a monthly basis according to the GRACE time span for comparison with GRACE-based vertical displacements. To remove the systematic differences between different datasets, each monthly series was centered by subtracting its mean over the valid months of the common study period. The resulting monthly GNSS vertical displacement series were defined as positive upward. Therefore, an increase in water mass loading generally corresponds to negative displacement, whereas water loss produces positive displacement.

2.2.2. GRACE/GRACE-FO TWSA

Monthly terrestrial water storage anomaly (TWSA) data were obtained from the RL06.2 GRACE/GRACE-FO Level-3 mascon product developed by the Center for Space Research (CSR) at the University of Texas at Austin (https://earth.gsfc.nasa.gov/geo/data/grace (accessed on 11 December 2024)). Although the product is distributed on a 0.25° grid, the grid spacing represents the sampling interval rather than the effective spatial resolution of the GRACE/GRACE-FO observations. Monthly data from February 2012 to November 2023 were used to match the availability of the GNSS observations. The GRACE TWSA data were converted into vertical displacements at the 15 GNSS stations using the Green's functions described in Section 2.3. Comparisons of vertical displacements between GRACE estimates and GNSS observations were conducted only for months in which both datasets were available.

2.2.3. GLDAS Noah TWSA

Land surface model data were obtained from NASA's Global Land Data Assimilation System (GLDAS). GLDAS uses observational and reanalysis meteorological data to drive land surface models and provides spatially and temporally consistent estimates of land surface states and fluxes [36]. This study used the 0.25°, 3-hourly GLDAS-2.1 Noah product [12]. For each grid cell, Noah-derived TWS was calculated as the sum of soil moisture (SM) in four layers, snow water equivalent (SWE), and canopy water storage (CWS) [13,37]:

$$TWS = SM + SWE + CWS \quad (1)$$

The 3-hourly Noah estimates were aggregated into monthly means based on the GRACE data time span. Following the GRACE processing procedure, the mean TWS for 2004–2009 was subtracted from each grid-cell time series to obtain Noah TWSA. The resulting TWSA data were converted into vertical displacements at the GNSS stations using the same Green's function approach as those applied to the GRACE data (Section 2.3).

2.2.4. Auxiliary Datasets

Precipitation and evapotranspiration data were used to interpret the hydrological processes underlying differences among the GNSS-, GRACE-, and Noah-derived displacements. Precipitation (P) was obtained from the Integrated Multi-satellitE Retrievals for the Global Precipitation Measurement mission (IMERG). The IMERG Version 7 Final Run daily precipitation product, which incorporates gauge-based bias correction, was used at a spatial resolution of 0.1°. The daily data was accumulated to monthly totals to ensure consistency with the processed monthly vertical displacement data.

Actual evapotranspiration (ET) was obtained from the Global Land Evaporation Amsterdam Model (GLEAM) Version 4.3, which has a spatial resolution of 0.1° and a monthly temporal resolution. GLEAM combines satellite observations with meteorological forcing to estimate total ET and its components, including vegetation transpiration, soil evaporation, canopy-interception evaporation, open-water evaporation, and snow sublimation [38]. GLEAM has been widely used as a reference dataset for evaluating model- and satellite-based ET estimates because it has undergone validation against eddy-covariance observations and generally performs well across different climatic regions and land cover types [38–40].

2.3. Green's Functions

Variations in terrestrial water storage redistribute surface mass and induce elastic deformation of the solid Earth. According to elastic loading theory, deformation caused by a spatially distributed surface load can be calculated by convolving the load with the corresponding load Green's functions [15,17]. Following Wahr et al. [41].each gridded load was approximated as a uniform circular disk. For a disk with an angular radius of α, the disk-integrated vertical response to a unit surface load at an angular distance λ from the disk center is:

$$dr(\lambda) = \sum_{l=0}^{\infty} h_l{}' \Gamma_l \frac{4\pi GR}{g(2l+1)} P_l(\cos\lambda) \quad (2)$$

where G is the gravitational constant, R is the mean radius of the Earth, g is the gravitational acceleration at the Earth's surface, P_l is the Legendre polynomial of degree l, and $h_l{}'$ is the load Love number describing the elastic vertical response of the solid Earth. In this study, load Love numbers based on the Preliminary Reference Earth Model (PREM) were used [42], and $h_1' = -0.269$ was used, corresponding to the center of figure (CF) frame [43]. The coefficient Γ_l, which accounts for the finite spatial extent of the circular load, is defined as:

$$\Gamma_l = \frac{1}{2}[P_{l-1}(\cos\alpha) - P_{l+1}(\cos\alpha)] \quad l > 0 \quad (3)$$

$$\Gamma_0 = \frac{1}{2}(1 - \cos\alpha) \quad (4)$$

Each 0.25° GRACE or Noah grid cell was approximated as a uniform circular disk with a radius of 14 km, corresponding to α = 14 km/R. A reference load of H_0 = 1 m equivalent water height (EWH) was used to calculate the unit disk response:

$$dr_\alpha^{H_0}(\lambda) = \rho_w H_0 dr(\lambda) \quad (5)$$

where ρ_w is the density of water. Because the elastic response is linear, the vertical displacement at station s and time t was calculated by scaling this unit response according to the TWSA of each grid cell and summing the contributions from all land grid cells globally:

$$dr_s(t) = \sum_{j\epsilon land} \frac{\Delta H_j(t)}{H_0} dr_\alpha^{H_0}(\lambda_{sj}) = \rho_w \sum_{j\epsilon land} \Delta H_j(t)\, dr(\lambda_{sj}) \quad (6)$$

where $\Delta H_j(t)$ is the TWSA of grid cell j, and λ_{sj} is the angular distance between the center of grid cell j and station s. Thus, the implementation does not More details on the calculation of point-scale displacement from gridded TWSA are provided in Wahr et al. [41].

Before conversion, both TWSA datasets were re-referenced by removing the temporal mean of each grid cell time series over the common study period from February 2012 to November 2023. This step was used to ensure a consistent zero reference and remove constant offsets between different datasets. The conversion of GRACE- and Noah-derived TWSA into vertical displacements enables direct comparison with the corrected GNSS observations.

2.4. STL Time-Series Decomposition

Seasonal and Trend decomposition using LOESS (STL) was applied to the monthly vertical displacement series derived from GNSS, GRACE, and Noah to separate low-frequency and seasonal variations. Each time series $u(t)$ was decomposed into three additive components:

$$u(t) = T(t) + S(t) + R(t) \quad (7)$$

where $T(t)$ represents the nonlinear low-frequency component, representing primarily interannual variability; $S(t)$ is the seasonal component with a 12-month period; and $R(t)$ is the remainder, containing short-term variability and unexplained noise. The seasonal and trend smoother lengths were set to 7 and 23 months, respectively. A low-pass smoother length of 13 months was used, with robust fitting enabled. To maintain a complete and regularly spaced monthly series, missing GRACE months, including the gaps between the GRACE and GRACE-FO missions, were filled using the multi-year mean for the corresponding month calculated from the available GRACE observations. The same STL parameter settings were applied to all vertical displacement datasets to ensure that the resulting components were directly comparable.

2.5. Statistical Evaluation Metrics

Agreement among GNSS-, GRACE-, and Noah-derived vertical displacements was evaluated using the processed monthly displacement time series and their STL-derived low-frequency and seasonal components. All pairwise comparisons were restricted to months with valid observations in both datasets. The Pearson correlation coefficient (r) was used to quantify the linear relationship between two time series:

$$r_{A,B} = \frac{\sum_{t=1}^{n}(A_t - \bar{A})(B_t - \bar{B})}{\sqrt{\sum_{t=1}^{n}(A_t - \bar{A})^2}\sqrt{\sum_{t=1}^{n}(B_t - \bar{B})^2}} \quad (8)$$

where A and B represent vertical displacements from different datasets, $\bar{A}$ and $\bar{B}$ are their respective means, and n is the number of common estimates. A larger positive r indicates greater similarity in temporal variations. However, the correlation coefficient is insensitive to additive offsets and amplitude scaling. A high correlation therefore does not necessarily indicate agreement in displacement magnitude.

Root-mean-square reduction (RMSR) was used as a complementary metric to evaluate agreement in both temporal variation and displacement magnitude. Taking A as the reference series and B as the comparison series, RMSR was calculated as:

$$RMS(x) = \sqrt{\frac{1}{n}\sum_{t=1}^{n} x_t^2} \quad (9)$$

$$RMSR_{A,B} = \frac{RMS(A) - RMS(A-B)}{RMS(A)} \times 100\% \quad (10)$$

where $RMS(A)$ denotes the RMS of dataset A, and $RMS(A-B)$ is the RMS of the residual after subtracting dataset B from dataset A. A Positive $RMSR$ indicates that subtracting B reduces the RMS variability of the reference series A, whereas a value approaching 100% indicates close agreement in both timing and magnitude. An RMSR of zero indicates no reduction in variability, while a negative value indicates that the residual series has a larger RMS than the original reference series.

3. Results

3.1. Comparison of Monthly Vertical Displacements

Network-mean vertical displacements were calculated by averaging the GNSS-, GRACE-, and Noah-derived estimates across the 15 station locations (Figure 2). The three series exhibited broadly similar temporal variations but differed substantially in magnitude and short-term variability. GNSS showed the greatest variability, followed by GRACE and Noah. The Pearson correlation coefficients (r) for GNSS–GRACE, GNSS–Noah, and GRACE–Noah were 0.48, 0.49, and 0.74, respectively. Thus, GNSS showed a similar level of agreement with GRACE and Noah, whereas the higher GRACE–Noah correlation indicated closer agreement between their regional monthly variations.

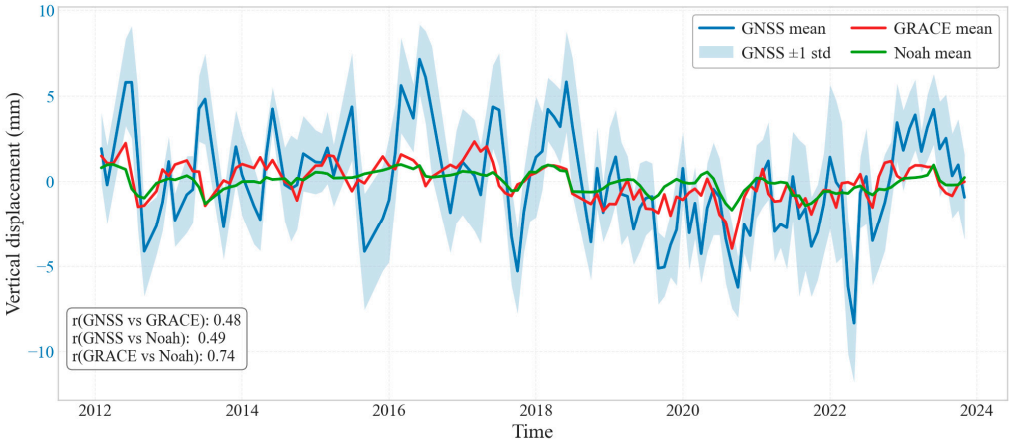


Figure 2. Monthly mean vertical displacements derived from GNSS, GRACE, and Noah. The shaded area denotes ±1 standard deviation of the GNSS observations across the 15-station network.

Station-level agreement varied markedly across the study area (Figure 3a–c). Correlations were generally higher at stations outside of the Heihe River Basin in the south. Most correlations at the five stations inside the basin were below 0.4 for all three pairwise comparisons. The mean station-level correlation was highest for GRACE-Noah (r = 0.60), compared with 0.38 for GNSS-GRACE and 0.35 for GNSS-Noah. These results reveal a pronounced contrast between stations inside and outside the basin. For the five stations inside the basin, the corresponding mean correlations were 0.16, 0.13, and 0.43 for the GNSS-GRACE, GNSS-Noah, and GRACE-Noah, respectively, compared with 0.49, 0.46, and 0.69 for the ten stations outside the basin. These differences may reflect regional differences in hydrological variability as well as data-specific uncertainties.

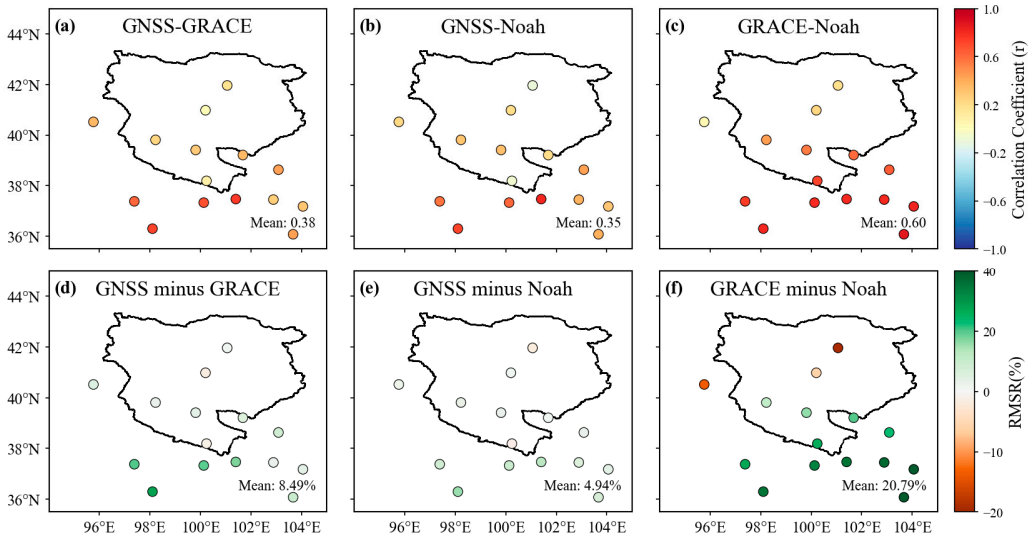


Figure 3. Spatial distributions of the Pearson correlation coefficients between (**a**) GNSS and GRACE, (**b**) GNSS and Noah, and (**c**) GRACE and Noah. Panels (**d**–**f**) show the corresponding RMS reductions obtained by subtracting GRACE from GNSS, Noah from GNSS, and Noah from GRACE, respectively.

The RMSR results showed similar spatial variations (Figure 3d–f). Subtracting the GRACE- and Noah-derived displacements from the GNSS series generally produced small positive or near-zero RMSR values, with station averages of 8.49% and 4.94%, respectively. The GRACE-Noah comparison showed greater consistency, with a mean RMSR of 20.79% after subtracting Noah from GRACE. For the ten stations outside the basin, the corresponding values were 12.17%, 7.03%, and 28.43% for the GNSS-GRACE, GNSS-Noah, and GRACE-Noah, respectively, whereas those for the five stations inside the basin were 1.12%, 0.75%, and 5.52%. The largest positive RMSR values occurred at stations south of the basin, whereas strongly negative values were found at several stations in the lower reaches. These results further demonstrate that the network-wide averages are influenced by the contrasting behavior of stations inside and outside the basin.

Overall, agreement among the GNSS-, GRACE-, and Noah-derived vertical displacements ranged from weak to moderate and varied considerably across the study area. Stations located outside the Heihe River Basin in the south generally showed greater consistency in both magnitude and phase, whereas substantial discrepancies occurred at the five stations located within the basin, particularly in the arid lower reaches. Potential explanations for these differences are discussed in Section 4.

3.2. Analysis of the Interannual and Seasonal Variations

STL decomposition was applied to the GNSS-, GRACE-, and Noah-derived vertical displacements at each station to separate their low-frequency, seasonal, and residual components. Figure 4 shows the spatial distribution of the correlations calculated for the low-frequency and seasonal components. For the low-frequency component, hereafter referred to as the interannual component, the highest station-average correlation was observed between GNSS and GRACE (r = 0.73), followed by GRACE-Noah (r = 0.61) and GNSS-Noah (r = 0.51). These correlations were higher than the corresponding values calculated from the original monthly time series in Section 3.1, particularly for the GNSS-GRACE comparison, suggesting a higher agreement at the interannual scale. The interannual correlations with Noah remained low for stations within the basin, but larger correlations were observed at stations south of the basin. The GNSS-GRACE correlations showed a less distinct spatial pattern.

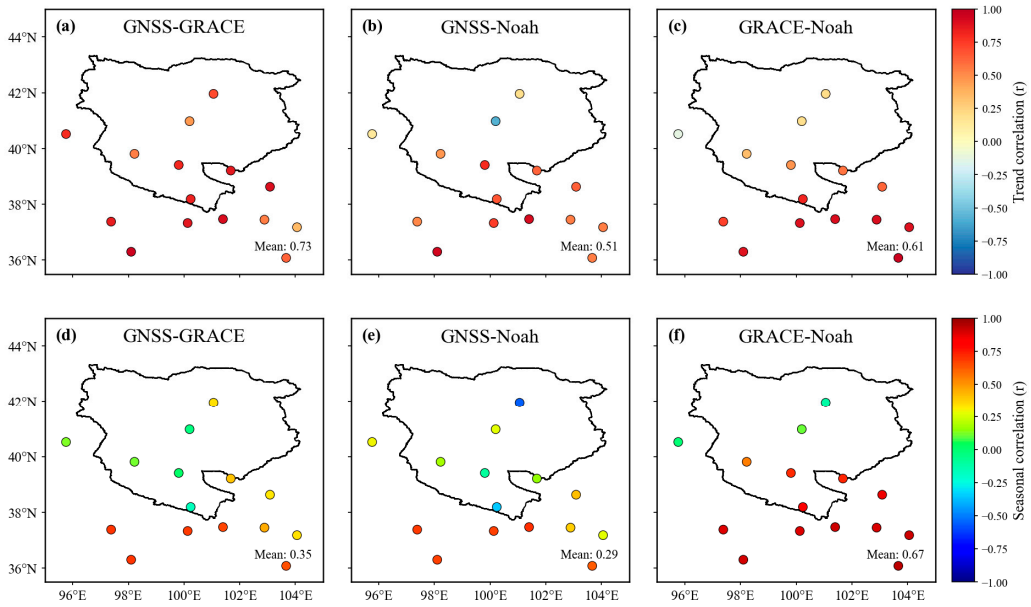


Figure 4. Spatial distributions of the Pearson correlation coefficients between the STL-derived low-frequency components of (**a**) GNSS and GRACE, (**b**) GNSS and Noah, and (**c**) GRACE and Noah. Panels (**d**–**f**) show the corresponding correlations between the seasonal components.

Agreement was substantially weaker for the seasonal components for GNSS comparisons (Figure 4d–f). Across all stations, the station-average seasonal correlations were 0.35 for GNSS–GRACE and 0.29 for GNSS–Noah, indicating limited seasonal agreement. In comparison, the GRACE-Noah correlation was higher at 0.67. For the five stations inside the basin, the corresponding correlations were 0.05, −0.11, and 0.42 for GNSS-GRACE, GNSS-Noah, and GRACE-Noah, respectively, compared with 0.50, 0.49, and 0.79 for stations outside the basin. To further analyze the differences among GNSS-, GRACE-, and Noah-derived vertical displacements at seasonal scale, the peak-to-peak amplitudes and peak months were compared.

Seasonal peak-to-peak amplitudes were further calculated from the multi-year mean seasonal cycles (Figure 5a–c). The station-mean amplitudes derived from GNSS, GRACE, and Noah were 7.98 ± 1.94, 1.89 ± 0.72, and 1.24 ± 0.51 mm, respectively, where the uncertainties represent one standard deviation across the 15 stations. The mean GNSS amplitude was approximately 4.22 times that of GRACE and 6.44 times that of Noah and was the largest at all stations. For all three datasets, seasonal amplitudes tended to be smaller at stations within the arid basin. The larger and more spatially variable GNSS amplitudes are consistent with previous findings [44] and may reflect its greater sensitivity to local loading, together with residual station-specific hydrological or non-hydrological signals. The smaller GRACE and Noah amplitudes may partly result from spatial smoothing and differences in the representation of water storage components.

For each station, the month of maximum uplift was identified from the maximum value of its multi-year mean STL seasonal cycle. Because displacement is positive upward, this month generally corresponds to minimum seasonal water loading. GNSS peak months varied widely among stations, ranging from approximately January to July and showing limited spatial coherence (Figure 5d). In contrast, the GRACE- and Noah-derived peaks were concentrated between March and June and generally occurred progressively later from south to north (Figure 5e,f). Relative to GRACE and Noah, GNSS tended to peak earlier at southern stations and later at northern stations, leading to poor seasonal correlation between GNSS and the other two datasets.

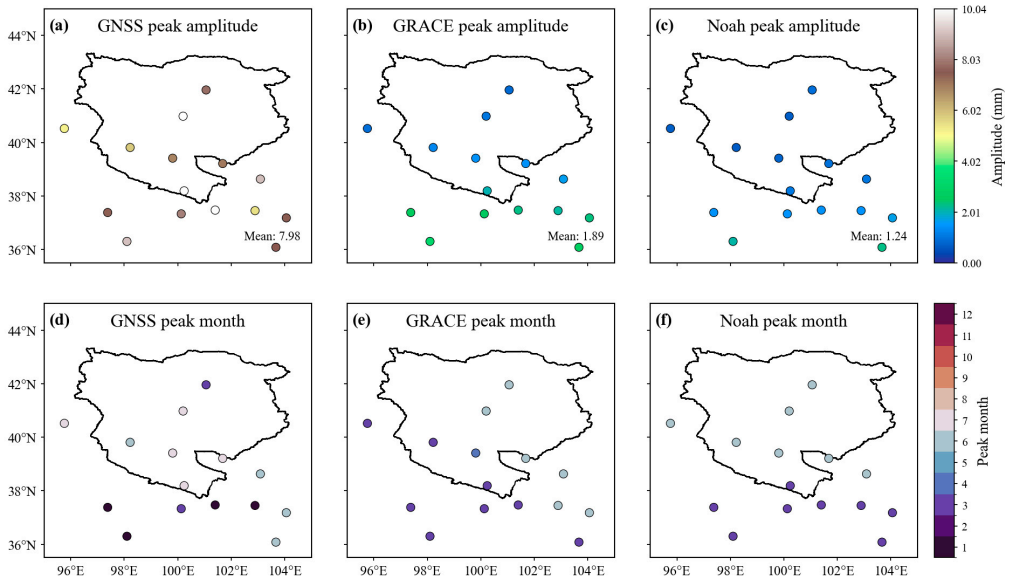


Figure 5. Spatial distributions of the seasonal peak-to-peak amplitudes derived from (**a**) GNSS, (**b**) GRACE, and (**c**) Noah. Panels (**d**–**f**) show the corresponding peak months of the multi-year mean seasonal cycles.

Overall, GNSS and GRACE showed the strongest agreement at interannual variability, whereas GRACE and Noah agreed more in seasonal timing and spatial pattern. GNSS exhibited substantially larger seasonal amplitudes, more dispersed peak months, and weak seasonal correlations with both GRACE and Noah. The potential effects of spatial sensitivity, differences in represented water storage components, and residual non-hydrological signals are discussed in Section 4.

4. Discussion

4.1. Sources of Interannual Discrepancies in Noah-Based Displacements

At the interannual timescale, Noah-based vertical displacements showed relatively weak agreement with both GNSS and GRACE, particularly at stations within the Heihe River Basin (Figure 4a–c). To determine whether this disagreement originated from differences in the underlying water storage fields, the STL-derived interannual components of GRACE and Noah TWSA were compared directly. The basin-averaged series show some agreement in the direction of change, particularly the decline after 2019, but greatly differed during the earlier period (Figure 6a). GRACE exhibited a gradual TWS decline from 2012 to 2017 followed by a short recovery during 2018–2019, whereas Noah showed a slight increase from 2012 to 2019. Consequently, the basin-averaged interannual GRACE and Noah TWSA components were moderately correlated ($r = 0.54$), indicating partial agreement between the two datasets. Because the same loading calculation was applied to both datasets, this result indicates that their displacement discrepancies originated primarily from differences in the simulated and observed water storage variations.

The spatial correspondence between GRACE and Noah also varied across the study area (Figure 6b). Interannual TWSA correlations were consistently positive south of the basin, moderate to high in its central part, and negative across much of the arid north. This distribution was broadly consistent with the station-level correlations between the GRACE- and Noah-derived vertical displacement. The temporal standard deviations of the interannual TWSA components provide further evidence of differences between the two datasets (Figure 6c,d). Both GRACE and Noah showed greater variability in the south and weaker variations in the arid north. However, GRACE displays a broader and

smoother spatial gradient, whereas the areas of high variability in Noah were more localized. The mean temporal standard deviation across the displayed area was 13.53 mm for GRACE and 9.57 mm for Noah. Noah showed particularly weak variability in the Badain Jaran Desert and the lower reaches of the Heihe River Basin. These results indicate that Noah produced more strongly damped interannual TWS variations than GRACE in arid regions. Nevertheless, the coarser effective resolution of GRACE, together with spatial leakage and boundary effects, may also contribute to the differences between the two products. GRACE should therefore not be regarded as an error-free reference.

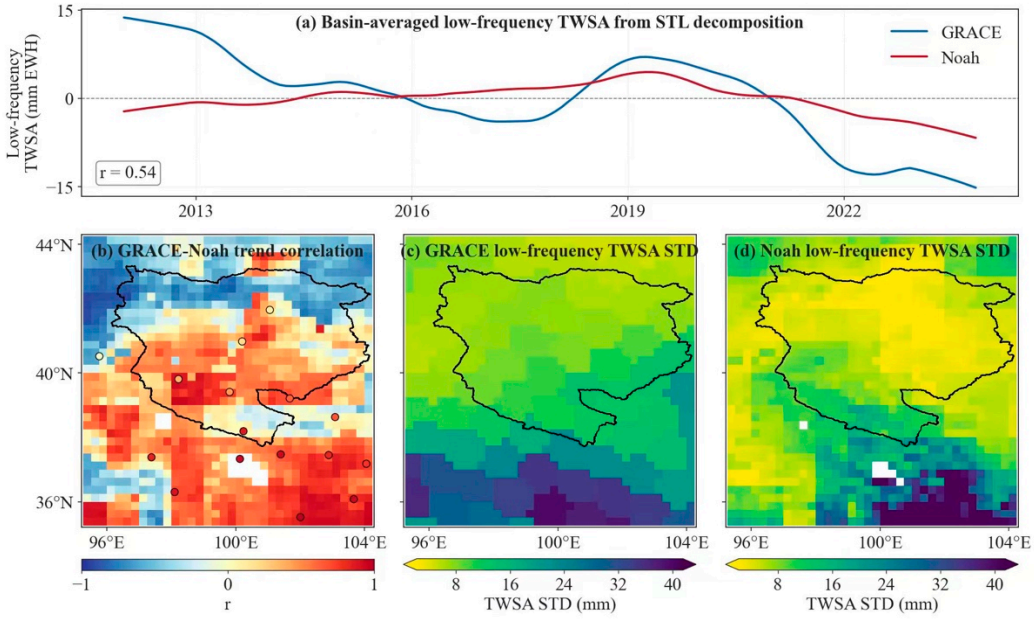


Figure 6. (**a**) Low-frequency components of GRACE- and Noah-derived TWSA spatially averaged over the Heihe River Basin. (**b**) Spatial distributions of the correlations between the low-frequency TWSA components from GRACE and Noah, with station-level correlations between the corresponding vertical displacements overlaid. (**c**,**d**) represent spatial distributions of the temporal standard deviations of low-frequency TWSA components derived from GRACE and Noah, respectively.

The reduced interannual variability of Noah TWSA in the arid part of the basin suggests that regional water fluxes may not be fully represented by the model. Because evapotranspiration is a major water loss component in this region, Noah-derived ET was compared with GLEAM as a preliminary assessment of one possible source of the discrepancy. GLEAM generally showed higher long-term mean ET and greater temporal variability than Noah (Figure 7). In GLEAM, relatively higher ET occurred in the Zhangye Basin, along the Heihe River, and in the western regions, whereas lower ET was observed in the Badain Jaran Desert in the east of the basin. In comparison, Noah simulated a more spatially homogeneous pattern. A lower mean ET in Noah could reduce simulated water loss and thereby lead to greater water retention, whereas its smaller temporal variability could contribute to the subdued interannual variability of Noah TWSA. However, it should be noted that although GLEAM has been evaluated against flux tower observations and other ET products in previous studies [38,39], its uncertainty within the basin has not been quantified. These interpretations remain hypotheses, as changes in storage also depend on precipitation, runoff, groundwater and surface water exchange, and human water management.

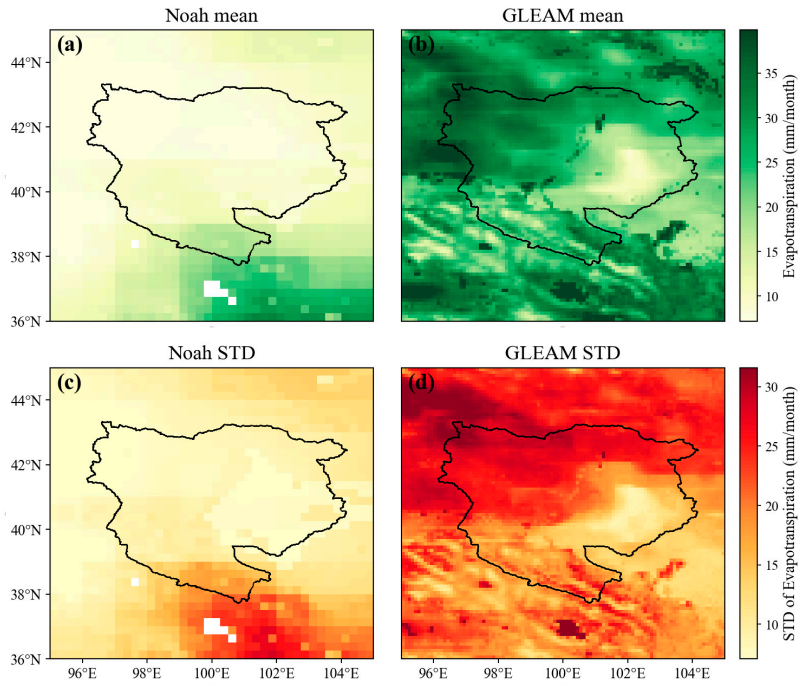


Figure 7. (**a**,**b**) Spatial distributions of mean evapotranspiration derived from (**a**) Noah and (**b**) GLEAM. Panels (**c**,**d**) represent the corresponding temporal standard deviations from Noah and GLEAM.

Differences in the represented water storage components provide an additional explanation. GRACE responds to changes in total terrestrial water mass, whereas Noah-derived TWSA includes only soil moisture, snow water equivalent, and canopy water storage. Groundwater, surface water, irrigation redistribution, and other water management processes are absent or incompletely represented in Noah [45], although these components are particularly important in the middle and lower reaches of the Heihe River Basin. Therefore, the lack of representation of these processes may suppress interannual variability in Noah and contribute to the low agreement with GRACE within the basin.

The higher interannual correlation of GNSS with GRACE than with Noah provides independent evidence that Noah did not fully reproduce the observed water storage dynamics. Overall, the Noah discrepancies may reflect a combination of differences in ET representation, omitted water storage components, and human water management. Their individual contributions cannot be separated using the current datasets. Further attribution requires precipitation, ET, runoff, groundwater, reservoir, and irrigation data evaluated over consistent spatiotemporal scales.

4.2. Potential and Limitations of GNSS for Monitoring TWS Variability

The comparison of GNSS-, GRACE-, and Noah-derived vertical displacements showed a consistent north–south contrast, with lower correlations for the stations within the basin in the north. The contrast was particularly pronounced at the seasonal scale, where several stations in the northern and lower reaches of the basin showed low or negative correlations, whereas higher correlations generally occurred at the southern stations. The spatial contrast may partly reflect the pronounced hydroclimatic gradient between the Qilian Mountains and the arid northern basin. Seasonal snow accumulation and melt in the southern mountains produce a relatively strong and spatially coherent loading and unloading cycle. The stronger hydrological signal may be resolved more consistently by GNSS, GRACE, and Noah, thereby contributing to the higher agreement. In contrast, the weaker regional water mass variations in the arid northern basin may reduce the signal-

to-noise ratio and increase the relative importance of localized hydrological processes. Groundwater-related deformation may provide another explanation for the relatively low agreement within the basin. Groundwater pumping and recharge can produce poroelastic deformation, while intensive pumping may cause irreversible aquifer system compaction. GNSS stations overlying affected aquifers may therefore record localized deformation that is not produced solely by elastic surface loading and may not be represented in the GRACE- and Noah-derived displacements. However, the contribution of these processes cannot be quantified due to the lack of local aquifer properties and groundwater management.

Despite these spatial differences, the agreement of GNSS with GRACE and Noah was generally higher at the interannual scale than at the seasonal scale. The moderate interannual agreement indicates that GNSS contains a measurable low-frequency hydrological loading signal. At the seasonal scale, GNSS generally exhibited larger amplitudes and greater station-to-station variability in peak timing. The relatively subdued seasonal displacements derived from GRACE and Noah are consistent with the weak regional TWS variations in arid environments, where precipitation is limited and large evaporative losses are high [44]. However, the larger GNSS amplitudes do not necessarily represent a more accurate estimate of hydrological loading, because the three datasets differ in spatial sensitivity and sources of uncertainty.

Differences in effective spatial support may partly explain the weaker seasonal agreement. GNSS vertical displacement represents the integrated elastic response to surrounding hydrological loads but is weighted more strongly toward nearby mass variations, making individual stations sensitive to localized mass changes. GRACE spatially smooths mass variations over several hundred kilometers, whereas Noah represents hydrological processes at the model-grid scale using spatially averaged forcing and parameterizations. Converting GRACE and Noah estimates to vertical displacement using Green's functions does not recover hydrological variability not solved by their original spatial representation. Consequently, localized and heterogeneous seasonal loading may produce larger amplitudes and more variable peak timing in GNSS than in GRACE- or Noah-derived displacements. Conversely, the relatively weak GRACE signal-to-noise ratio in arid regions, uncertainties in Noah's representation of hydrological processes, and residual non-hydrological signals in GNSS may all contribute to the observed discrepancies [46,47]. These complementary sensitivities suggest that GNSS can provide an additional constraint on gridded TWSA estimates rather than serve as a direct substitute for GRACE or land surface models.

Lagged correlations were calculated using the complete processed monthly displacement series without STL decomposition to further characterize the overall temporal alignment among the three datasets. Lags from −6 to +6 months were examined, and the lag corresponding to the maximum Pearson correlation was selected (Figure 8). For each ordered comparison, a positive lag indicates that the second dataset leads the first. Larger lags are generally observed at northern stations in the GNSS-GRACE and GNSS-Noah comparisons, particularly those located near river channels or runoff convergence zones. This suggests that the variations represented by GRACE and Noah tended to precede those observed by GNSS. In contrast, the optimal lags between GRACE and Noah were close to zero at most stations, indicating closer temporal alignment between these two datasets.

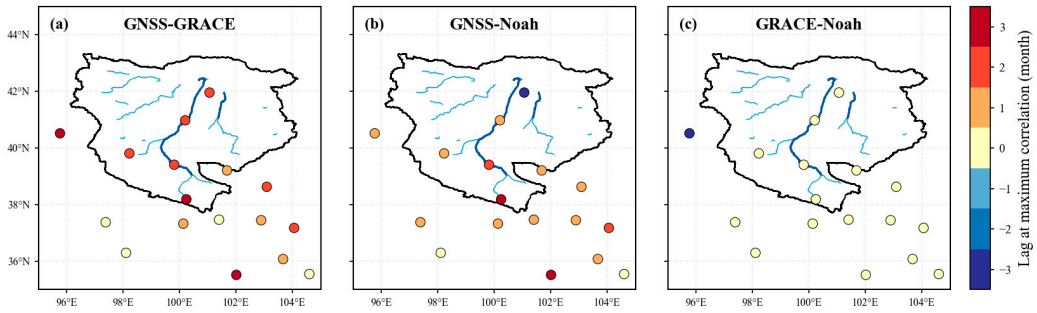


Figure 8. Spatial distributions of the optimal time lags associated with the maximum pairwise correlations in vertical displacements between (**a**) GNSS and GRACE, (**b**) GNSS and Noah, and (**c**) GRACE and Noah.

One possible explanation for the time lags between GNSS and GRACE (or Noah) is the combined effect of downstream water redistribution and the different spatial sensitivities of the datasets. Streamflow in the Heihe River Basin generally reaches its maximum during July-August [48], whereas basin-scale TWS tends to be relatively high during the transition from spring to summer [47]. Water detected earlier as a basin-scale storage change may subsequently be redistributed toward the northern and lower reaches through infiltration, runoff routing, and groundwater recharge, causing delayed local water mass changes. Because GNSS deformation is influenced more strongly by nearby loads, although it also integrates loading over a broader area, this delayed local redistribution could shift the GNSS time series relative to the spatially smoothed GRACE and Noah estimates. Additionally, similar lags could also arise from spatial averaging in GRACE, model uncertainty in Noah, differences in signal-to-noise ratio, or residual non-hydrological signals in GNSS. The spatial pattern of the lags should only be used as suggestive evidence that localized hydrological processes may contribute to the seasonal timing differences among the datasets. Interpretation of its seasonal signal requires additional information on local hydrological conditions and independent observations of river flow, groundwater, soil moisture, and irrigation.

5. Conclusions

This study compared vertical displacements derived from GNSS, GRACE, and Noah at 15 stations within and surrounding the Heihe River Basin using consistent monthly sampling and station locations. Regional averaging improved the agreement among datasets, with GRACE and Noah showing the strongest correlation at the monthly scale. GNSS exhibited moderate agreement with both GRACE and Noah at regional scale, whereas station-level correlations exhibited pronounced spatial variability. Agreement between GNSS and the other datasets was generally weaker at stations in the lower reaches.

STL decomposition revealed clear timescale-dependent differences. At the interannual scale, GNSS and GRACE showed relatively consistent variations, with a station-averaged correlation of 0.73. Noah differed substantially from both GRACE and GNSS, particularly at stations within the Heihe River Basin. The deteriorated interannual consistency between Noah and GRACE or GNSS may be related to the inadequate representation of deep groundwater and human water use. Comparisons between Noah- and GLEAM-based evapotranspiration further suggest that potential biases in simulated water fluxes may contribute to these discrepancies.

At the seasonal scale, GNSS exhibited weak correlations with GRACE and Noah. GRACE and Noah produced relatively subdued seasonal displacements, whereas GNSS exhibited substantially larger amplitudes and greater spatial variability in peaking time.

These discrepancies may reflect the greater sensitivity of GNSS to nearby and spatially heterogeneous loads, which are smoothed in GRACE or incompletely represented by Noah. However, residual non-hydrological signals, station instability, and non-elastic deformation may also contribute to the larger GNSS seasonal amplitudes. Seasonal GNSS variations should therefore not be interpreted directly as local TWS changes without additional constraints.

Overall, GNSS provides an independent deformation constraint that complements GRACE observations and Noah simulations, particularly at the interannual scale. Integrating GNSS with satellite gravimetry and land surface models offers a promising approach for identifying inconsistencies among datasets. The study used the CSR mascon product as a representative GRACE solution. However, differences among GRACE products arising from their distinct parameterizations, regularization strategies, and post-processing procedures remain a source of uncertainty. Future work should quantify these differences among products on the GRACE-derived displacements at individual GNSS stations. Joint inversion and data assimilation frameworks should also be explored to combine these complementary datasets to improve TWSA estimates and the representation of hydrological processes in arid inland river basins.

Author Contributions: Conceptualization, G.Y. and J.M.; methodology, G.Y., J.M. and J.B.; software, J.M. and Y.G.; validation, J.M., Y.G. and J.P.; resources, G.Y., Y.N. and R.Z.; data curation, J.P. and Y.N.; writing—original draft preparation, J.M.; writing—review and editing, Y.G., J.P., G.Y.; visualization, J.M.; supervision, J.B., G.Y.; funding acquisition, G.Y. and R.Z. All authors have read and agreed to the published version of the manuscript.

Funding: The research was funded by the Joint Open Fund of Water Cycle Field Station of the Heihe River Basin, CGS (No. WCSHR-2024-10), Education Department of Jilin Province (No. JJKH20250126KJ), Natural Science Foundation of Gansu Province (No. 25JRRG011), and Zhangye Major Technical Tackling Project (ZY2024JBGS08).

Data Availability Statement: The daily GNSS vertical displacement data are archived by the National Earthquake Science Data Center of China (https://data.earthquake.cn/ (accessed on 24 December 2025)). The GRACE/GRACE-FO mascon product are obtained from the Center for Space Research at the University of Texas at Austin (https://www2.csr.utexas.edu/grace/ (accessed on 11 November 2024)). The GLDAS Noah version 2.1 data were obtained from the NASA Goddard Earth Sciences Data and Information Services Center (GES DISC; https://disc.gsfc.nasa.gov/ (accessed on 22 October 2026)). The IMERG Version 07 Final precipitation data are acquired from https://gpm.nasa.gov/data/directory (accessed on 22 October 2026). The Global Land Evaporation Amsterdam Model (GLEAM) version 4.3 evapotranspiration data are obtained from the GLEAM data portal (https://www.gleam.eu/ (accessed on 15 April 2026)). The digital elevation model data used for mapping and spatial analysis were obtained from the Geospatial Data Cloud (https://www.gscloud.cn/ (accessed on 15 April 2026)). The processed GNSS time series, Green's-function-derived vertical displacement data, and statistical results generated in this study are available from the corresponding author upon reasonable request, subject to the data-use policies of the original data providers.

Conflicts of Interest: The authors declare no conflicts of interest.

References

1. Tapley, B.D.; Bettadpur, S.; Ries, J.C.; Thompson, P.F.; Watkins, M.M. GRACE Measurements of Mass Variability in the Earth System. *Science* **2004**, *305*, 503–505. https://doi.org/10.1126/science.1099192.
2. Humphrey, V.; Gudmundsson, L.; Seneviratne, S.I. Assessing Global Water Storage Variability from GRACE: Trends, Seasonal Cycle, Subseasonal Anomalies and Extremes. *Surv. Geophys.* **2016**, *37*, 357–395. https://doi.org/10.1007/s10712-016-9367-1.

3. Wada, Y.; Van Beek, L.P.H.; Van Kempen, C.M.; Reckman, J.W.T.M.; Vasak, S.; Bierkens, M.F.P. Global Depletion of Groundwater Resources. *Geophys. Res. Lett.* **2010**, *37*, L20402. https://doi.org/10.1029/2010GL044571.
4. Cosgrove, W.J.; Loucks, D.P. Water Management: Current and Future Challenges and Research Directions. *Water Resour. Res.* **2015**, *51*, 4823–4839. https://doi.org/10.1002/2014WR016869.
5. Chang, L.; Yuan, R.; Gupta, H.V.; Winter, C.L.; Niu, G. Why Is the Terrestrial Water Storage in Dryland Regions Declining? A Perspective Based on Gravity Recovery and Climate Experiment Satellite Observations and Noah Land Surface Model With Multiparameterization Schemes Model Simulations. *Water Resour. Res.* **2020**, *56*, e2020WR027102. https://doi.org/10.1029/2020WR027102.
6. An, L.; Wang, J.; Huang, J.; Pokhrel, Y.; Hugonnet, R.; Wada, Y.; Cáceres, D.; Müller Schmied, H.; Song, C.; Berthier, E.; et al. Divergent Causes of Terrestrial Water Storage Decline Between Drylands and Humid Regions Globally. *Geophys. Res. Lett.* **2021**, *48*, e2021GL095035. https://doi.org/10.1029/2021GL095035.
7. Zhao, K.; Li, X. Estimating Terrestrial Water Storage Changes in the Tarim River Basin Using GRACE Data. *Geophys. J. Int.* **2017**, *211*, 1449–1460. https://doi.org/10.1093/gji/ggx378.
8. Zhang, M.; Wang, S.; Fu, B.; Gao, G.; Shen, Q. Ecological Effects and Potential Risks of the Water Diversion Project in the Heihe River Basin. *Sci. Total Environ.* **2018**, *619–620*, 794–803. https://doi.org/10.1016/j.scitotenv.2017.11.037.
9. Zhang, Y.; Lu, Y.; Zhou, Q.; Wu, F. Optimal Water Allocation Scheme Based on Trade-Offs between Economic and Ecological Water Demands in the Heihe River Basin of Northwest China. *Sci. Total Environ.* **2020**, *703*, 134958. https://doi.org/10.1016/j.scitotenv.2019.134958.
10. Li, X.; Cheng, G.; Ge, Y.; Li, H.; Han, F.; Hu, X.; Tian, W.; Tian, Y.; Pan, X.; Nian, Y.; et al. Hydrological Cycle in the Heihe River Basin and Its Implication for Water Resource Management in Endorheic Basins. *J. Geophys. Res. Atmos.* **2018**, *123*, 890–914. https://doi.org/10.1002/2017JD027889.
11. Save, H.; Bettadpur, S.; Tapley, B.D. High-resolution CSR GRACE RL05 Mascons. *J. Geophys. Res. Solid Earth* **2016**, *121*, 7547–7569. https://doi.org/10.1002/2016JB013007.
12. Beaudoing, H.; Rodell, M.; Hydrological Sciences Laboratory (HSL). *GLDAS Noah Land Surface Model L4 3 Hourly 0.25 x 0.25 Degree, Version 2.1*; NASA Goddard Earth Sciences Data and Information Services Center: Greenbelt, MD, USA, 2020.
13. Cai, X.; Yang, Z.; Xia, Y.; Huang, M.; Wei, H.; Leung, L.R.; Ek, M.B. Assessment of Simulated Water Balance from Noah, Noah-MP, CLM, and VIC over CONUS Using the NLDAS Test Bed. *J. Geophys. Res. Atmos.* **2014**, *119*, 13751–13770. https://doi.org/10.1002/2014JD022113.
14. Van Dam, T.; Wahr, J.; Milly, P.C.D.; Shmakin, A.B.; Blewitt, G.; Lavallée, D.; Larson, K.M. Crustal Displacements Due to Continental Water Loading. *Geophys. Res. Lett.* **2001**, *28*, 651–654. https://doi.org/10.1029/2000GL012120.
15. Farrell, W.E. Deformation of the Earth by Surface Loads. *Rev. Geophys.* **1972**, *10*, 761–797. https://doi.org/10.1029/RG010i003p00761.
16. Knowles, L.A.; Bennett, R.A.; Harig, C. Vertical Displacements of the Amazon Basin From GRACE and GPS. *J. Geophys. Res. Solid Earth* **2020**, *125*, e2019JB018105. https://doi.org/10.1029/2019JB018105.
17. Yin, G.; Forman, B.A.; Loomis, B.D.; Luthcke, S.B. Comparison of Vertical Surface Deformation Estimates Derived From Space-Based Gravimetry, Ground-Based GPS, and Model-Based Hydrologic Loading Over Snow-Dominated Watersheds in the United States. *J. Geophys. Res. Solid Earth* **2020**, *125*, e2020JB019432. https://doi.org/10.1029/2020JB019432.
18. Zhang, R.; Peng, Y.; Chao, N.; Ou, Q.; Chen, G.; Wang, Z.; Zhu, H.; Liu, B.; Zhang, Z. A Rapid Increase of Groundwater in 2021 over the North China Plain from GPS and GRACE Observations. *GPS Solut.* **2025**, *29*, 37. https://doi.org/10.1007/s10291-024-01794-5.
19. Carlson, G.; Werth, S.; Shirzaei, M. A Novel Hybrid GNSS, GRACE, and InSAR Joint Inversion Approach to Constrain Water Loss during a Record-Setting Drought in California. *Remote Sens. Environ.* **2024**, *311*, 114303. https://doi.org/10.1016/j.rse.2024.114303.
20. Borsa, A.A.; Agnew, D.C.; Cayan, D.R. Ongoing Drought-Induced Uplift in the Western United States. *Science* **2014**, *345*, 1587–1590. https://doi.org/10.1126/science.1260279.
21. Chanard, K.; Avouac, J.P.; Ramillien, G.; Genrich, J. Modeling Deformation Induced by Seasonal Variations of Continental Water in the Himalaya Region: Sensitivity to Earth Elastic Structure. *J. Geophys. Res. Solid Earth* **2014**, *119*, 5097–5113. https://doi.org/10.1002/2013JB010451.
22. Bevis, M.; Alsdorf, D.; Kendrick, E.; Fortes, L.P.; Forsberg, B.; Smalley, R.; Becker, J. Seasonal Fluctuations in the Mass of the Amazon River System and Earth's Elastic Response. *Geophys. Res. Lett.* **2005**, *32*, L16308. https://doi.org/10.1029/2005GL023491.

23. Su, G.; Zhan, W. Seasonal and Long-Term Vertical Land Motion in Southwest China Determined Using GPS, GRACE, and Surface Loading Model. *Earth Planets Space* **2021**, *73*, 131. https://doi.org/10.1186/s40623-021-01459-4.
24. Chen, Y.; Niu, J.; Kang, S.; Zhang, X. Effects of Irrigation on Water and Energy Balances in the Heihe River Basin Using VIC Model under Different Irrigation Scenarios. *Sci. Total Environ.* **2018**, *645*, 1183–1193. https://doi.org/10.1016/j.scitotenv.2018.07.254.
25. Liu, M.; Xu, X.; Jiang, Y.; Huang, Q.; Huo, Z.; Huang, G. An Integrated Hydrological Model for the Restoration of Ecosystems in Arid Regions: Application in Zhangye Basin of the Middle Heihe River Basin, Northwest China. *J. Geophys. Res. Atmos.* **2018**, *123*, 12564–12582. https://doi.org/10.1029/2018JD028449.
26. Cao, X.; Hu, X.; Pan, B.; Zhao, Z. Spatiotemporal Variation of Late Quaternary River Incision Along the Heihe River in the Northeastern Tibetan Plateau, Constrained by Dating Fluvial Terraces. *Front. Earth Sci.* **2022**, *10*, 929599. https://doi.org/10.3389/feart.2022.929599.
27. Liu, S.; Li, X.; Xu, Z.; Che, T.; Xiao, Q.; Ma, M.; Liu, Q.; Jin, R.; Guo, J.; Wang, L.; et al. The Heihe Integrated Observatory Network: A Basin-Scale Land Surface Processes Observatory in China. *Vadose Zone J.* **2018**, *17*, 1–21. https://doi.org/10.2136/vzj2018.04.0072.
28. Feng, Q.; Cheng, G.D.; Endo, K.N. Towards Sustainable Development of the Environmentally Degraded River Heihe Basin, China. *Hydrol. Sci. J.* **2001**, *46*, 647–658. https://doi.org/10.1080/02626660109492862.
29. Zang, C.; Liu, J. Trend Analysis for the Flows of Green and Blue Water in the Heihe River Basin, Northwestern China. *J. Hydrol.* **2013**, *502*, 27–36. https://doi.org/10.1016/j.jhydrol.2013.08.022.
30. Sun, W.; Song, H.; Yao, X.; Ishidaira, H.; Xu, Z. Changes in Remotely Sensed Vegetation Growth Trend in the Heihe Basin of Arid Northwestern China. *PLoS ONE* **2015**, *10*, e0135376. https://doi.org/10.1371/journal.pone.0135376.
31. Chew, C.C.; Small, E.E. Terrestrial Water Storage Response to the 2012 Drought Estimated from GPS Vertical Position Anomalies. *Geophys. Res. Lett.* **2014**, *41*, 6145–6151. https://doi.org/10.1002/2014GL061206.
32. Han, S.; Razeghi, S.M. GPS Recovery of Daily Hydrologic and Atmospheric Mass Variation: A Methodology and Results From the Australian Continent. *J. Geophys. Res. Solid Earth* **2017**, *122*, 9328–9343. https://doi.org/10.1002/2017JB014603.
33. Li, X.; Zhong, B.; Li, J.; Liu, R. Joint Inversion of GNSS and GRACE/GFO Data for Terrestrial Water Storage Changes in the Yangtze River Basin. *Geophys. J. Int.* **2023**, *233*, 1596–1616. https://doi.org/10.1093/gji/ggad014.
34. Dobslaw, H.; Bergmann-Wolf, I.; Dill, R.; Poropat, L.; Thomas, M.; Dahle, C.; Esselborn, S.; König, R.; Flechtner, F. A New High-Resolution Model of Non-Tidal Atmosphere and Ocean Mass Variability for de-Aliasing of Satellite Gravity Observations: AOD1B RL06. *Geophys. J. Int.* **2017**, *211*, 263–269. https://doi.org/10.1093/gji/ggx302.
35. Yan, H.; Chen, W.; Zhu, Y.; Zhang, W.; Zhong, M. Contributions of Thermal Expansion of Monuments and Nearby Bedrock to Observed GPS Height Changes. *Geophys. Res. Lett.* **2009**, *36*, L13301. https://doi.org/10.1029/2009GL038152.
36. Rodell, M.; Houser, P.R.; Jambor, U.; Gottschalck, J.; Mitchell, K.; Meng, C.-J.; Arsenault, K.; Cosgrove, B.; Radakovich, J.; Bosilovich, M.; et al. The Global Land Data Assimilation System. *Bull. Am. Meteorol. Soc.* **2004**, *85*, 381–394. https://doi.org/10.1175/BAMS-85-3-381.
37. Scanlon, B.R.; Zhang, Z.; Rateb, A.; Sun, A.; Wiese, D.; Save, H.; Beaudoing, H.; Lo, M.H.; Müller-Schmied, H.; Döll, P.; et al. Tracking Seasonal Fluctuations in Land Water Storage Using Global Models and GRACE Satellites. *Geophys. Res. Lett.* **2019**, *46*, 5254–5264. https://doi.org/10.1029/2018GL081836.
38. Miralles, D.G.; Holmes, T.R.H.; De Jeu, R.A.M.; Gash, J.H.; Meesters, A.G.C.A.; Dolman, A.J. Global Land-Surface Evaporation Estimated from Satellite-Based Observations. *Hydrol. Earth Syst. Sci.* **2011**, *15*, 453–469. https://doi.org/10.5194/hess-15-453-2011.
39. Miralles, D.G.; Bonte, O.; Koppa, A.; Baez-Villanueva, O.M.; Tronquo, E.; Zhong, F.; Beck, H.E.; Hulsman, P.; Dorigo, W.; Verhoest, N.E.C.; et al. GLEAM4: Global Land Evaporation and Soil Moisture Dataset at 0.1° Resolution from 1980 to near Present. *Sci. Data* **2025**, *12*, 416. https://doi.org/10.1038/s41597-025-04610-y.
40. Bai, P.; Liu, X. Intercomparison and Evaluation of Three Global High-Resolution Evapotranspiration Products across China. *J. Hydrol.* **2018**, *566*, 743–755. https://doi.org/10.1016/j.jhydrol.2018.09.065.
41. Wahr, J.; Khan, S.A.; Van Dam, T.; Liu, L.; Van Angelen, J.H.; Van Den Broeke, M.R.; Meertens, C.M. The Use of GPS Horizontals for Loading Studies, with Applications to Northern California and Southeast Greenland. *J. Geophys. Res. Solid Earth* **2013**, *118*, 1795–1806. https://doi.org/10.1002/jgrb.50104.
42. Wang, H.; Xiang, L.; Jia, L.; Jiang, L.; Wang, Z.; Hu, B.; Gao, P. Load Love Numbers and Green's Functions for Elastic Earth Models PREM, Iasp91, Ak135, and Modified Models with Refined Crustal Structure from Crust 2.0. *Comput. Geosci.* **2012**, *49*, 190–199. https://doi.org/10.1016/j.cageo.2012.06.022.

43. Kusche, J.; Schrama, E.J.O. Surface Mass Redistribution Inversion from Global GPS Deformation and Gravity Recovery and Climate Experiment (GRACE) Gravity Data. *J. Geophys. Res. Solid Earth* **2005**, *110*, B09409. https://doi.org/10.1029/2004JB003556.
44. Chen, T.; Pan, Y.; Jiao, J.; He, M. Integrating GNSS and GRACE Observations to Investigate Water Storage Variations Across Different Climatic Regions of China. *IEEE Trans. Geosci. Remote Sens.* **2025**, *63*, 1–15. https://doi.org/10.1109/TGRS.2025.3563095.
45. Syed, T.H.; Famiglietti, J.S.; Rodell, M.; Chen, J.; Wilson, C.R. Analysis of Terrestrial Water Storage Changes from GRACE and GLDAS. *Water Resour. Res.* **2008**, *44*, W02433. https://doi.org/10.1029/2006WR005779.
46. Scanlon, B.R.; Zhang, Z.; Save, H.; Sun, A.Y.; Müller Schmied, H.; Van Beek, L.P.H.; Wiese, D.N.; Wada, Y.; Long, D.; Reedy, R.C.; et al. Global Models Underestimate Large Decadal Declining and Rising Water Storage Trends Relative to GRACE Satellite Data. *Proc. Natl. Acad. Sci. USA* **2018**, *115*, E1080–E1089. https://doi.org/10.1073/pnas.1704665115.
47. Cao, Y.; Nan, Z.; Cheng, G. GRACE Gravity Satellite Observations of Terrestrial Water Storage Changes for Drought Characterization in the Arid Land of Northwestern China. *Remote Sens.* **2015**, *7*, 1021–1047. https://doi.org/10.3390/rs70101021.
48. Zhang, A.; Zheng, C.; Wang, S.; Yao, Y. Analysis of Streamflow Variations in the Heihe River Basin, Northwest China: Trends, Abrupt Changes, Driving Factors and Ecological Influences. *J. Hydrol. Reg. Stud.* **2015**, *3*, 106–124. https://doi.org/10.1016/j.ejrh.2014.10.005.

Disclaimer/Publisher's Note: The statements, opinions and data contained in all publications are solely those of the individual author(s) and contributor(s) and not of MDPI and/or the editor(s). MDPI and/or the editor(s) disclaim responsibility for any injury to people or property resulting from any ideas, methods, instructions or products referred to in the content.